DEVELOPMENT OF AN IMPEDANCE MODEL FOR THE ISIS SYNCHROTRON AND PREDICTIONS FOR THE HEAD-TAIL INSTABILITY

D. W. Posthuma de Boer[*,1], B. A. Orton, C. M. Warsop, R. E. Williamson

ISIS Neutron and Muon Source, Harwell, UK

[1]also at John Adams Institute, Oxford, UK

Abstract

ISIS is the pulsed, spallation neutron and muon source at the Rutherford Appleton Laboratory in the UK. The rapid cycling synchrotron which drives the facility accelerates 3×10^{13} protons-per-pulse from 70 to 800 MeV at 50 Hz, and delivers a mean beam power of 0.2 MW to two target stations. Beam-loss mechanisms must be understood to optimise performance and minimise equipment activation and to develop mitigation methods for future operations and new accelerators.

Substantial beam-losses are driven by a vertical head-tail instability which has also limited beam intensity. Beam-based impedance measurements suggest the instability is driven by a low frequency narrowband impedance but its physical origin remains unknown. More generally, research into the nature of the instability is hindered without a detailed transverse impedance model.

This paper presents a survey of low frequency vertical impedance estimates for ISIS equipment, using analytical methods, CST simulations and lab-based coil measurements. The final impedance estimate is then used as an input to a new linearised Vlasov solver, and predicted growth rates compared with previously obtained experimental results.

INTRODUCTION

The ISIS Neutron and Muon Source has been successfully operating for close to 40 years. Key parameters of the rapid cycling synchrotron (RCS) which drives the facility are listed in Table 1. Its dual harmonic RF system captures and accelerates up to 3×10^{13} protons with a repetition rate of 50 Hz, producing a mean beam power of 0.2 MW. Following extraction, accelerated protons are directed to one of two targets stations (TS1 and TS2), with beam to TS1 also intercepting an intermediate target for muon production.

ISIS has reported a vertical head-tail instability for more than three decades [1, 2]. In contrast with the observed mode 1 instability, indicated by the single node in the difference signal of Fig. 1, it was found that the sinusoidal mode approximation [3] predicted modes 2 or 3 to be most unstable. Measurements confirmed that the growth rate grew as vertical tune approached an integer ($Q_y \sim 3.83 \rightarrow 4$), supporting a theory that the instability was driven by resistive wall [2]. However, with a thick resistive wall model, simplified instability theories [4] predicted growth times on the

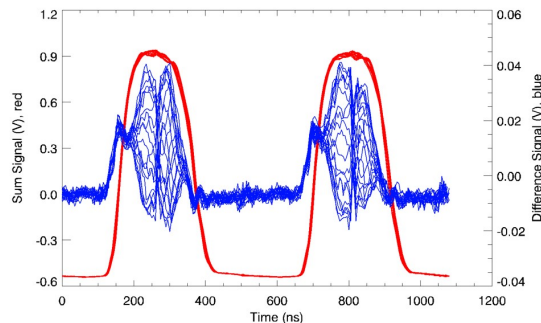---
* david.posthuma-de-boer@stfc.ac.uk

Figure 1: Position monitor sum (red) and difference (blue) signals, taken close to 2 ms into the synchrotron acceleration cycle during routine operations [10].

order of ms, whilst the instability grew with characteristic times on the order of 100 µs.

These apparent contradictions between theory and observation motivated an extensive measurement campaign [5–11] an alternative formulation of transverse bunched-beam instabilities [12], and the development of an experimental damping system [13]. Measurements of real effective transverse impedance with a coasting beam, have hinted at the existence of a 85 kHz narrowband impedance, which was subsequently corroborated by measurements of head-tail growth rate versus vertical tune; see Fig. 2 [8].

Table 1: Key ISIS Synchrotron Parameters

Property	Value
Kinetic Energy Range	70 - 800 MeV
Number of Bunches (M)	2
Circumference	163.3 m
No. of Superperiods	10
Gamma Transition	5.034
Nominal Tunes (Q_x, Q_y)	4.31, 3.83 (variable)
Peak Incoherent Tune Shift	Exceeding $\sim$ -0.5 [8]
Chromaticity (ξ_x, ξ_y)	-1.4, -1.4
No. of RF Cavities (h = 2,4)	6, 4
Injection Scheme	H$^-$ charge-exchange
Extraction Scheme	Single-turn, vertical

This paper will develop an improved low frequency resistive wall impedance model with modern analytical and numerical methods to specific equipment within the ISIS synchrotron. This will then be compared with the thick resistive wall model that has been applied until now. Res-
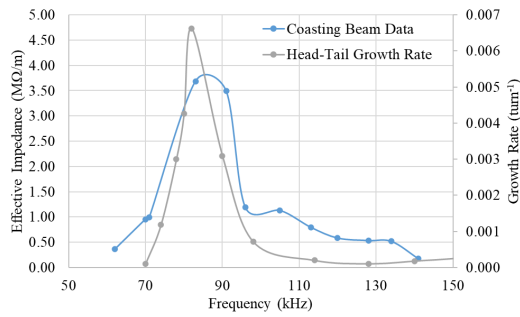
Figure 2: Effective impedance measured with a coasting beam, and overlaid with head-tail growth rate measurements made with a bunched, stored beam [10].

onator impedances on ISIS will also be analysed using low frequency CST simulations and lab-based probe coil measurements. Experimental results are shown for the vertical extraction kickers, and preliminary results from ongoing measurements on magnet RF screens are also presented. A new, open-source Vlasov solver, PyTMCI is introduced and applied with the updated impedance model.

VERTICAL IMPEDANCE MODEL

The vertical dipolar impedance model at ISIS has previously used a standard thick wall approximation for a cylindrical stainless steel pipe with an aperture of 50 mm [8], without considering inductive bypass, material thickness or cross-section [14–16]. This model can significantly over-or-under estimate the impedance at low frequencies. This uncertainty is exacerbated on ISIS by the complexity of its vacuum vessels [17] and uncharacterised material properties. As resistive wall was initially thought to be the sole driving impedance, a detailed analysis of the structures within ISIS has been performed, and the most significant contributors presented here. Possible sources of low frequency narrow-band impedance have also been investigated.

Multi-Layer Cylindrical Pipes

To investigate multi-layer vessels, a new code RWAL, was developed to find $Z_1^\perp(\omega)$ for multi-layer, concentric cylindrical pipes, using an existing formalism [18–20]. It uses a computer algebra system [21] to solve an EM field matching matrix, and avoids repeated solutions by storing optimised versions of the resulting formulae for up to five material layers to disk. RWAL was benchmarked against numerical results from low frequency CST simulations, which used a rectangular current loop as indicated in Fig. 3; to compute the imaginary part, $Z_1^\perp$ was also obtained for a pipe with a large conductivity and subtracted [22]. $Z_1^\perp(\omega)$ is shown for the case of a 2 mm thick, stainless steel vessel in free space. The methods are consistent at low frequency, whilst discrepancies are seen at higher frequencies, where meshing is unable to properly resolve the skin depth in CST.

Different combinations of conducting materials were investigated using RWAL. Figure 4 shows three cases, respec-
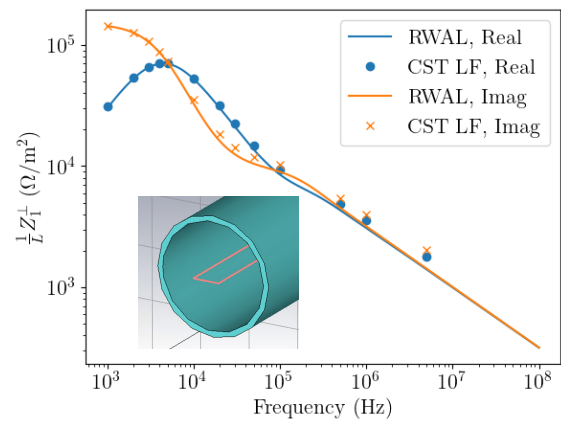

Figure 3: Benchmark for $Z_1^\perp(\omega)$ of a 2 mm thick stainless steel, cylindrical pipe in free space, computed with RWAL and a low frequency CST simulation.

tively a copper pipe in free space (case-1), the same pipe with a graphite outer layer extending to infinity (case-2) and the same outer layer without the copper pipe (case-3). Above 10 kHz, where the skin depth is close to the wall thickness, $Z_1^\perp(\omega)$ in case-2 is similar to case-1, because the copper screens all outer materials. At lower frequencies, fields begin to penetrate the copper and case-1 develops a $\frac{1}{f}$ dependence in the "Sacherer region" [15] before reaching a maxima and falling due to the inductive-bypass effect [14]. Case-3 also exhibits this effect, but its worse conductivity forces this to occur at a higher frequency. Because of this $Z_1^\perp(\omega)$ is very similar for cases-1 and 2, even at low frequencies where fields penetrate the cooper layer. From these cases we gain the qualitative understanding, that $Z_1^\perp$ is only slightly affected by structures whose inductive-bypass has been shielded by an inner layer.
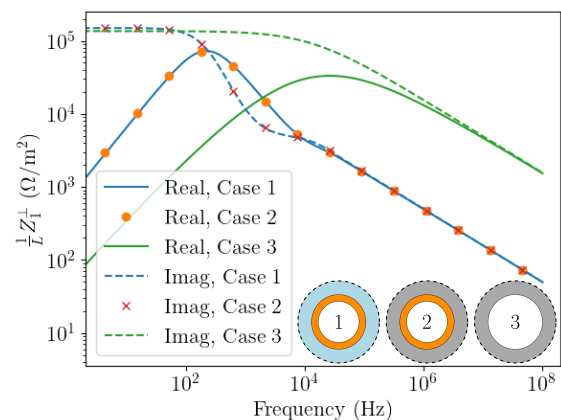

Figure 4: $Z_1^\perp(\omega)$ computed by RWAL for a copper pipe in free space (case-1), a copper pipe with an infinite graphite outer layer (case-2) and the same outer layer only (case-3). Inset indicates the geometry of each case.

RF Screen Resistive Wall

The AC magnet fields at ISIS preclude the use of typical stainless steel vacuum vessels in their vicinity, due to eddy current effects [23, 24]. Instead, alumina is used [17], and conducting RF screens inserted to shield the beams EM fields from outside structures; Fig. 5 schematically indicates their layout. These screens occupy nearly 55 % of the circumference, and primarily consist of 2.3 mm diameter, stainless steel wires, but side-plates are also used in the dipole magnets. To prevent eddy currents, each wire or side plate is capacitively coupled to the others at one end, which are expected to present a large impedance at 50 Hz, and a negligibly small impedance for beam-induced currents.
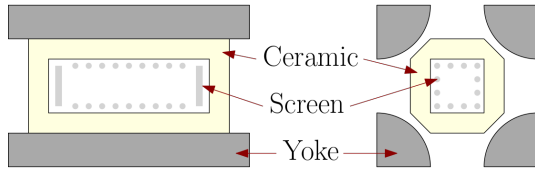

Figure 5: Schematic layout of magnet vacuum vessels for a dipole (left) and quadrupole (right). Higher multipole magnets have vessels which more closely resemble the quadrupole arrangement.

Neglecting the coupling capacitors, these structures somewhat resemble the multi-layer pipes which can be solved with RWAL, but with a laminated magnet outer layer. The yoke laminations are constructed from Transil 315-35, a silicon transformer steel. Their thickness of 350 μm limited the applicability of finite element methods, so analytical solutions for the yoke without an RF screen were investigated and benchmarked [25, 26]. The low frequency CST technique, already described, was used to benchmark the cylindrical lamination model [25]. Figure 6 shows a set of indicative results, demonstrating that CST reproduces the turning point and approximate magnitude of theoretical results, with some discrepancies attributed to imperfect meshing.
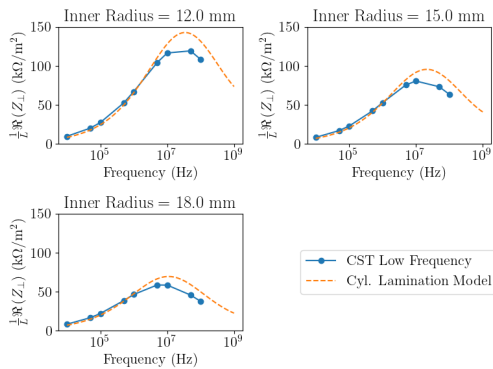

Figure 6: Indicative benchmarks of the circular lamination model [25] and low frequency CST simulations for different inner radii.

Figure 7 shows $Z_1^\perp(\omega)$ for a circular lamination model with Transil 315-35 laminations, where the inner radius was

made equal to the main dipole's smallest aperture. As the inductive-bypass frequency is close to 100 MHz, its contribution to $Z_1^\perp(\omega)$ at 100 kHz was considered negligible, and the yokes were subsequently neglected in RF screen simulations.
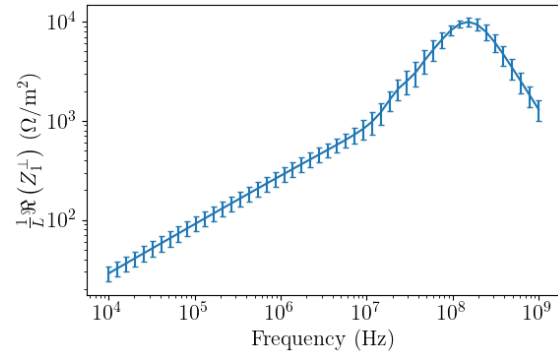

Figure 7: $Z_1^\perp(\omega)$ of an unshielded, laminated magnet yoke, computed with the circular lamination model [25] with a Yokoya factor of $\frac{\pi^2}{12}$ applied. Error bars account for estimated uncertainties in lamination thickness, spacing, permeability and conductivity.

Low frequency CST simulations were performed for the screens, with a large bounding box; the inset to Fig. 8 shows a model. The wires were 2 mm diameter and had a conductivity of $(1.33 \pm 0.01) \times 10^6 \, \text{S m}^{-1}$, as measured by an eddy current probe technique [27]. Perfect conducting loops shorted the wires together at both ends, emulating connections made on the real RF screens and providing a return path for the simulation. Figure 8 overlays $\Re\left(Z_1^\perp(\omega)\right)$ for the most common RF screens used on ISIS. An inductive-bypass turning point close to 5 kHz was observed in all cases, with Sacherer and surface impedance regions at higher frequencies [28]. A total is overlaid and the previous thick wall approximation scaled for length. This differs from the total by up to 15 % between 100 kHz and 10 MHz.
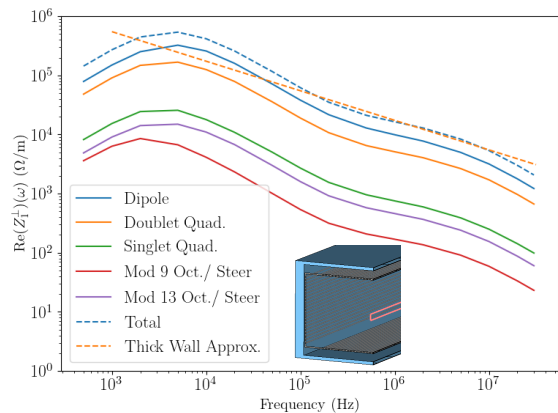

Figure 8: Resistive wall $\Re\left(Z_1^\perp(\omega)\right)$ for different RF screen families, neglecting the coupling capacitors.

RF Cavity Resistive Wall

Fundamental ($h = 2$) and second harmonic ($h = 4$) RF cavities make up ~15 % of the ISIS circumference. Their vacuum vessels are composed of mild steel with a nickel coating; its design provides magnetic shielding between the cavity ferrite's bias field and the beam [29]. The nickel coating is assumed to be 10-50 μm thick, but its conductivity and magnetic properties are not well known. Since published material data for nickel ranges so widely [30], RWAL has been used to analyse 3-layer models with a range of thicknesses, permeabilities (50-600) and conductivities (7×10^5 - 1.4×10^7 S m^{-1}). Properties were then taken which maximised the difference in $\Re\left(Z_1^\perp(\omega)\right)$ at the baseband betatron sideband and the first RF harmonic.
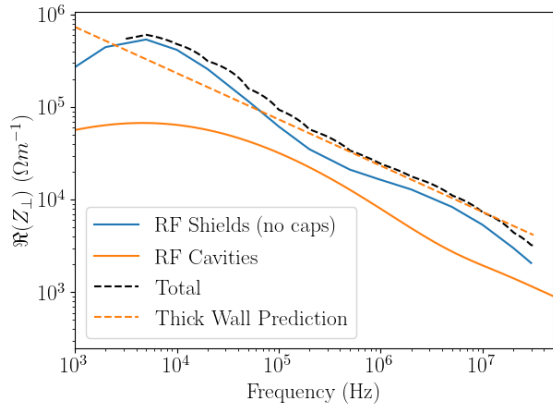

Figure 9: Predicted $\Re\left(Z_1^\perp(\omega)\right)$ for the RF cavity resistive wall, overlaid with the RF screen impedance, a total and original thick wall prediction, scaled for length.

The real part of the estimated impedance is overlaid with an interpolated total and the RF screen impedance in Fig. 9. Although the cavities are not the most significant contributor, their thin coating pushes up $\Re\left(Z_1^\perp(\omega)\right)$ at low frequencies, such that the combination of RF screens and cavities is ~ 30 % larger than the original thick wall approximation at 100 kHz.

Extract Kicker Narrowband Impedance

Kicker magnets are known to produce low frequency narrowband impedances in their operating plane, as the beams dipole moment couples to the external kicker cables and circuits [15, 31–33]. At ISIS, this has motivated a series of lab-based measurements on a spare kicker plus cable assembly.

ISIS has three vertical extraction kickers, whose construction are all similar apart from length variations. They are of a window-frame ferrite construction, with an Eddy current shield separating the two halves; see the inset of Fig. 12. Opposing plates are each fed by eight, ~90 m long, 50 Ω RG220 cables, as shown in Fig. 10. The plates are shorted together at the upstream end.

A single-turn probe loop [15] was inserted between the kicker plates, and measured using a Vector Network Analyser
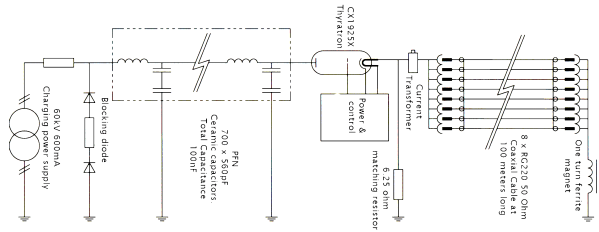

Figure 10: Circuit layout of a single extract kicker plate, with the pulse forming network, thyratron, terminating resistor, long cables and lumped-inductance kicker.

(VNA) as indicated in Fig. 11. The probe was treated as lumped and its impedance calculated with

$$Z_{\text{coil}} = Z_0 \frac{1 + S_{11}}{1 - S_{11}}, \tag{1}$$

where $Z_0 = 100\ \Omega$ is the characteristic impedance with the hybrid and S_{11} is the reflection scattering parameter [34]. $Z_1^\perp(\omega)$ was then obtained with

$$Z_1^\perp(\omega) = \frac{c}{\omega} \frac{Z_{\text{coil}}^{\text{DUT}} - Z_{\text{coil}}^{REF}}{\Delta^2 N^2}, \tag{2}$$

where Δ is the coil width and N is the number of turns [22]. Since low frequency resonances were of primary interest, $Z_{\text{coil}}^{\text{DUT}}$ was taken as the coil impedance with the probe inserted and the cables connected, and $Z_{\text{coil}}^{\text{REF}}$ was obtained by disconnecting the cables and shorting the kicker plates to the magnet body [31]. The probe was constructed from 3 mm diameter aluminium; the separation of their axes were assumed to define $\Delta = 20$ mm.
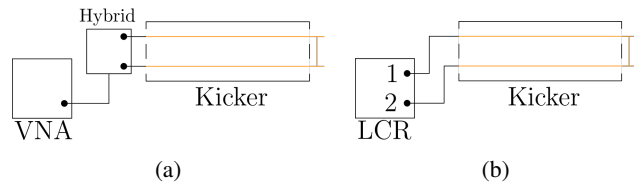

Figure 11: Experimental set-up for a loop-probe measured by a VNA (a) and an LCR meter (b).

Figure 12 shows $Z_1^\perp(\omega)$ measured with the cables disconnected from the matched terminating resistor. In this configuration resonances were observed at odd harmonics of quarter-wave intervals on the transmission line formed by the kicker and cables [32, 35]. With kicker and cable phase velocities of ~ 0.3c and 0.66c respectively, and assuming a kicker of length 1 m, the first resonance is expected at ~ 470 kHz. Given uncertainties in phase velocities at different parts of the system, this is considered consistent with the observed 440 kHz. With the matched terminating resistors connected, the first peak in $\Re\left(Z_1^\perp(\omega)\right)$ was shifted to 790 kHz, and reduced in magnitude from 42 kΩ m^{-1} to 3.5 kΩ m^{-1}; indicating that the resistor is successfully damping resonances on the cables. Comparing this magnitude with resistive wall, Fig. 9, justifies neglecting these kickers from the overall low frequency impedance model.
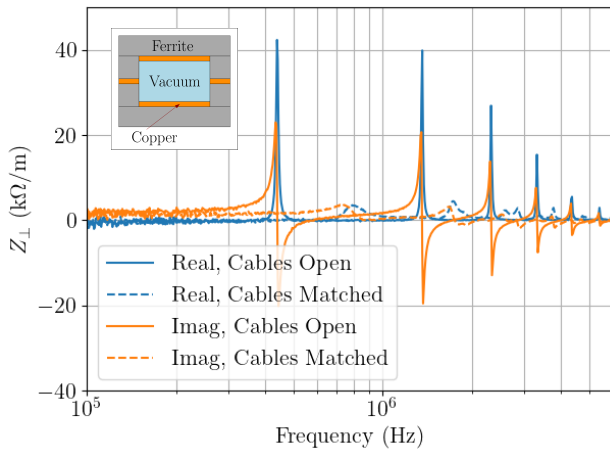
Figure 12: Measured $Z_1^\perp(\omega)$ of a spare extract kicker, with the cables disconnected from the matched terminating resistor (solid) and connected to it (dashed).

RF Screen Narrowband Impedance

The RF screen resistive wall impedances neglected the coupling capacitors. Simulations including these capacitors were carried out using the free space CST models previously described, with a 5 mm gap made in each wire and a lumped capacitor inserted. Figure 13 shows results for the most common screen families. Approximate resonator impedance properties [36] read from this figure are listed in Table 2.

Table 2: Estimates of Simulated RF Screen $Z_1^\perp$ Properties

RF Screen	$\frac{\omega_r}{2\pi}$ (kHz)	$R_\perp$ (MΩ m^{-1})	Q_r	**Quantity**
Dipole	300	1.3	15	10
Doublet	95	0.7	15	10
Singlet	185	0.26	30	10
Module 13	185	0.1	30	6
Module 9	160	0.07	30	6

These simulated results have motivated probe coil measurements on a spare singlet magnet, initially using the LCR meter set-up shown in Fig. 11 and two coil configurations. Whilst the experiment is ongoing, the preliminary results shown in Fig. 14 seem to confirm the existence of a narrowband impedance at 185 kHz. A smaller-than-predicted amplitude of 35 kΩ m^{-1} is observed, and a quality factor of $Q \approx 4.5$ provides a better fit than the value listed in Table 2. Such discrepancies are not unexpected, given the simplified geometry in CST. Additional measurements and refinement of the CST simulations are planned.

COHERENT TRANSVERSE BUNCHED BEAM INSTABILITIES

Sacherer's integral equation [3] has been widely adopted for the study of bunched-beam instabilities, and is given in Eq. (6.179) of [37]. For M equally spaced, identical bunches,
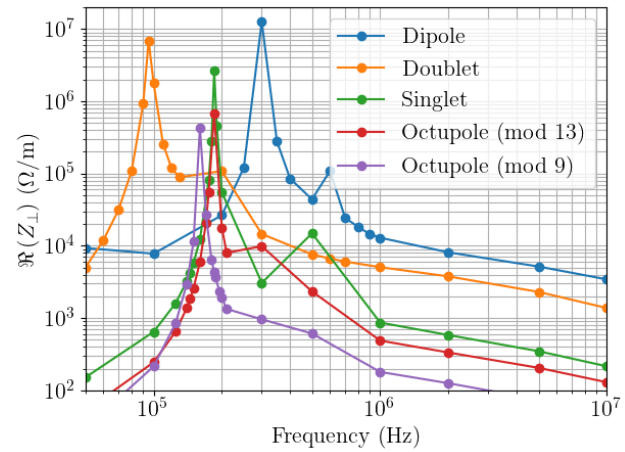
Figure 13: Simulated $Z_1^\perp(\omega)$ of the RF screens with capacitors included and yokes neglected.
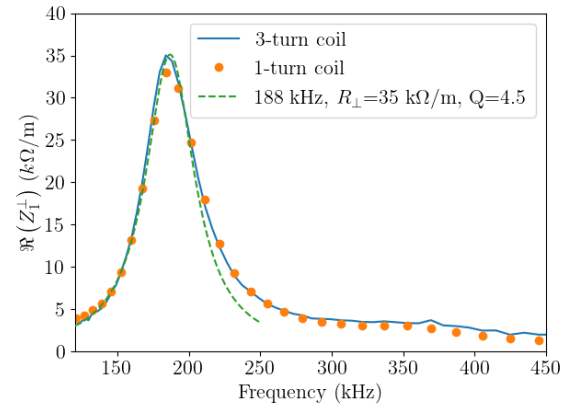

Figure 14: Preliminary results of a probe measurement of $\Re\left(Z_1^\perp(\omega)\right)$ for a singlet RF screen.

its $\beta \neq 1$ form is

$$\left(\Omega - \omega_\beta - \omega_s l\right) R_l(r) = \frac{-i\pi r_0 \omega_s M}{\beta^2 \gamma \omega_\beta T_0^2 \eta} g_0(r)$$

$$\times \sum_{l'=-\infty}^{\infty} i^{l-l'} \int_{r'=0}^{\infty} r' R_{l'}(r') \sum_{p=-\infty}^{\infty} Z_1^\perp(\omega')$$

$$\times J_{l'}\left(\frac{\omega' - \omega_\xi}{\beta c} r'\right) J_l\left(\frac{\omega' - \omega_\xi}{\beta c} r\right) dr', \quad (3)$$

with the same definitions as that reference, except $\beta \neq 1$ and α_l has been absorbed into $R_l(r)$. To write this in a form that is subject to eigen-analysis, this radial dependence of the perturbed distribution, $R_l(r)$, can be represented as a sum of generalised Laguerre polynomials [38], a sum of concentric delta functions (NHT) [39] or a single delta function [37]. To compute a mode frequency Ω, the RHS must be evaluated with $\omega' = (pM + \mu)\omega_0 + \Omega$. A perturbation approach results in the approximation $\omega' \approx (pM + \mu)\omega_0 + \omega_\beta + l\omega_s$, which is often shortened to $\omega' \approx (pM + \mu)\omega_0 + \omega_\beta$ on the basis that $\omega_\beta \gg \omega_s$. Alternatively, if $Z_1^\perp$ is sufficiently smooth, then it is possible to make the substitution $\sum_{p=-\infty}^{\infty} \to \frac{1}{M\omega_0} \int_{\omega'=-\infty}^{\infty} d\omega'$.
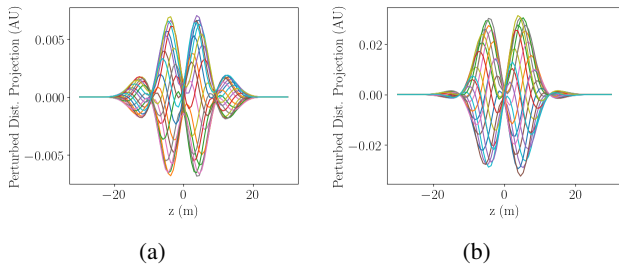
(a)   (b)

Figure 15: Longitudinal distribution of transverse dipole moment, predicted by PyTMCI for a thick wall impedance plus resonator impedances with properties either listed in Table 2 (a), or speculated based on experimental results.

A new head-tail Vlasov solver, PyTMCI [40], implements all of these longitudinal models, and methods to evaluate the RHS of Eq. 3; a single benchmark is listed in the Appendix. It will be used in the following section.

Head-Tail Predictions for ISIS

Whilst Fig. 9 shows differences between the assumed thick wall and actual resistive wall impedance, the resonant RF screen impedances dominate $Z_1^\perp(\omega)$ below around 500 kHz. Resistive wall differences are thus considered negligible, and the vertical driving impedance model will now consist of the original thick wall approximation plus five transverse resonators from the most common screen assemblies. The properties of these resonators are not yet certain, due to the discrepancy between simulations and preliminary measurements, but with the information now available, two approaches are taken. In the first, the simulated results listed in Table 2 are used directly, and in the second the measured singlet impedance is used to speculate a 7.5× reduction in $R_\perp$, and a 6.7× reduction in Q for all screens. PyTMCI is used with the parameters listed in Table 1 and $\beta = 0.45$, $Q_s = 0.015$, $N = 1.3 \times 10^{13}$ and a Gaussian longitudinal model with $\sigma_z = 6.5$ m. The first approach predicts mode -3 to be the most unstable, with a growth time of 440 µs; and the second approach predicts mode -1 to be the most unstable, with a growth time of 175 µs; Fig. 15 shows the predicted distributions for both models.

CONCLUSION

Low frequency CST simulations and RWAL computations have been used to develop a low frequency resistive wall, vertical driving impedance model for the ISIS synchrotron; the RF screens and RF cavities were found to be primary contributors. Probe coil measurements on a spare extraction kicker have verified that its termination resistors reduce the resonant impedances associated with its cables by an order-of-magnitude, and thus the kickers' contribution is considered negligible for the overall model at low frequencies. CST simulations have predicted large narrowband impedances due to the coupling capacitors in the RF screens, which dominate the impedance below ~ 500 kHz. Preliminary probe coil measurements on a singlet magnet RF screen

have identified a narrowband impedance at the predicted frequency, although its peak is wider than in simulation and its amplitude smaller. The final impedance model consists of a thick resistive wall impedance plus a resonator for each family of RF screens; although the resonator properties must still be ascertained with more sophisticated simulations and measurements. With this model, PyTMCI predicts growth times with the same order-of-magnitude as the 230 µs indicated by Fig. 2, and longitudinal distributions which more closely resemble those observed experimentally.

Future work will focus on RF screen measurements, simulations and an investigation of mitigation methods. Comparing beam observations with tracking simulations that include space-charge and more realistic RF buckets will also be a focus. Inclusion of detuning impedances and a refinement of the resistive wall model are longer term considerations, as is characterisation of the remaining equipment.

ACKNOWLEDGEMENTS

APPENDIX

PyTMCI Benchmark Example

PyTMCI and PyHEADTAIL [41] were used with the same parameters as given for the ISIS predictions, except with $\xi_y = -0.5$ and a single transverse resonator ($R_\perp = 1$ MΩ m^{-1}, $Q = 1$ and $\frac{\omega_r}{2\pi} = 2.4$ MHz). The resulting distributions are shown in Fig. 16, with eigenvalues computed by the Laguerre polynomial and NHT methods. PyTMCI predicts a growth time of 76 µs and PyHEADTAIL 72 µs.

(a)   (b)

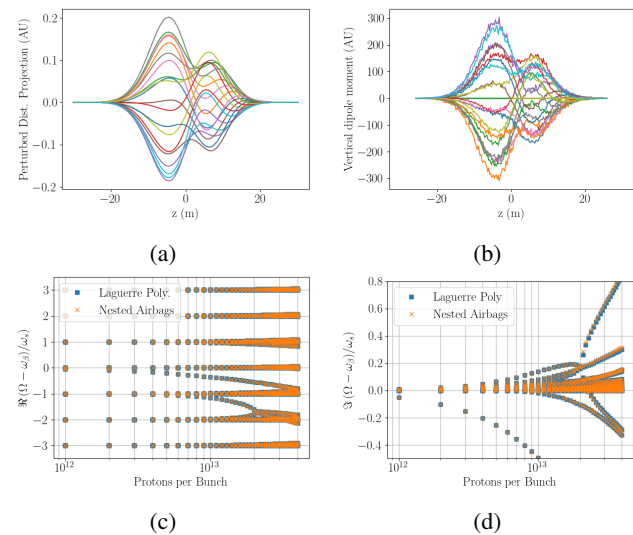(c)   (d)

Figure 16: Longitudinal distribution of transverse dipole moment computed with PyTMCI (a) and PyHEADTAIL (b). Real (c) and imaginary (d) parts of eigenvalues, computed by PyTMCI with different longitudinal models.

REFERENCES

[1] C. W. Planner, "Progress to operating at 100-microA on ISIS," in *1988 DPF Summer Study on High-energy Physics in the 1990s (Snowmass'88)*, Snowmass, CO, USA, Jun.-Jul. 1988, pp. 422–424.

[2] M. Harold *et al.*, "Diagnostics and commissioning progress on ISIS," in *Proc. EPAC'88*, Rome, Italy, Jun. 1988, pp. 347–349. https://accelconf.web.cern.ch/e88/PDF/EPAC1988_0347.PDF

[3] F. Sacherer, "Methods for computing bunched-beam instabilities," CERN, Geneva, Switzerland, Rep. CERN-SI-INT-BR-72-5, 1972. https://cds.cern.ch/record/2291670/

[4] F. J. Sacherer, "Transverse bunched-beam instabilities," CERN, Geneva, Switzerland, Rep. CERN-PS-BR-76-21, Nov. 1976. https://cds.cern.ch/record/322533/

[5] G. H. Rees, "Aspects of beam stability at ISIS," *AIP Conf. Proceedings*, vol. 496, no. 1, pp. 17–21, 1999. doi:10.1063/1.1301871

[6] C. M. Warsop, D. J. Adams, B. Jones, *et al.*, "High intensity loss mechanisms on the ISIS rapid cycling synchrotron," East Lansing, MI, USA, Nov. 2014, pp. 203–207. https://accelconf.web.cern.ch/HB2014/papers/tuo3lr03.pdf

[7] V. Kornilov *et al.*, "Thresholds of the Head-Tail Instability in Bunches with Space Charge," in *Proc. IBIC'14*, East Lansing, MI, USA, Nov. 2014, pp. 240–244. http://accelconf.web.cern.ch/AccelConf/HB2014/

[8] R. E. Williamson, B. Jones, and C. M. Warsop, "Development of Physics Models of the ISIS Head-Tail Instability," in *Proc. HB16*, 2016, pp. 155–159. http://accelconf.web.cern.ch/AccelConf/hb2016/papers/mopr031.pdf

[9] R. E. Williamson, B. Jones, A. Pertica, *et al.*, "Measurements and damping of the ISIS head-tail instability," in *Proc. ICFA mini-Workshop on Mitigation of Coherent Beam Instabilities in Particle Accelerators*, Zermatt, Switzerland, Sep. 2019, pp. 357–361. doi:10.23732/cyrcp-2020-009.357

[10] R. E. Williamson, "Studies of beam instabilities and associated beam-loss on a high-intensity proton synchrotron," PhD thesis, John Adams Institute, University of Oxford, UK, 2023.

[11] R. E. Williamson, D. J. Adams, and H. V. Cavanagh, "High-intensity studies on the ISIS RCS and their impact on the design of ISIS-II," presented at HB'23, Geneva, Switzerland, Oct. 2023, paper THA1I2, this conference.

[12] G. H. Rees, "Interpretation of the Higher Mode, Head-Tail Motion Observed on ISIS," *Part. Accel.*, vol. 39, pp. 159–167, 1992. http://cds.cern.ch/record/1108258/

[13] A. Pertica, J. Komppula, D. W. Posthuma de Boer, *et al.*, "Optimisation of the ISIS Proton Synchrotron experimental damping system," in *in Proc. IBIC'19*, Malmö, Sweden, Sep. 2019, pp. 167–171. doi:10.18429/JACoW-IBIC2019-MOPP031

[14] L. Vos, "The transverse impedance of a cylindrical pipe with arbitrary surface impedance," CERN, Geneva, Switzerland, Rep. CERN-ab-2003-005, 2003. http://cds.cern.ch/record/604828/

[15] G. Nassibian and F. Sacherer, "Methods for measuring transverse coupling impedances in circular accelerators," *Nucl. Instrum. Methods*, vol. 159, no. 1, pp. 21–27, 1979. doi:10.1016/0029-554X(79)90323-9

[16] K. Yokoya, "Resistive wall impedance of beam pipes of general cross section," *Part. Accel.*, vol. 41, pp. 221–248, 1993. https://cds.cern.ch/record/248630/

[17] I. Gardner, "The relevance of ISIS experience to the design of future high intensity synchrotrons," in *Part. Accel.*, vol. 31, 1990, pp. 227–234. http://cds.cern.ch/record/1108185/

[18] B. W. Zotter, "Transverse oscillations of a relativistic particle beam in a laminated vacuum chamber," CERN, Geneva, Switzerland, Rep. CERN 69-15, Jun. 1969. doi:10.5170/cern-1969-015

[19] R. Gluckstern, "Analytic Methods for Calculating Coupling Impedances," CERN, Geneva, Switzerland, Rep. CERN-ab-2000-001, 2000. doi:10.5170/cern-2000-011

[20] N. Mounet and E. Métral, "Impedances of two dimensional multilayer cylindrical and flat chambers in the non-ultrarelativistic case," in *Proc. HB'10*, Sep.-Oct. 2010, Morschach, Switzerland, pp. 353–357. https://accelconf.web.cern.ch/HB2010/papers/tuo1c02.pdf

[21] A. Meurer, C. P. Smith, M. Paprocki, *et al.*, "SymPy: Symbolic computing in Python," *PeerJ Comput. Sci.*, Jan. 2017. doi:10.7717/peerj-cs.103

[22] F. Roncarolo, "Comparison between laboratory measurements, simulations, and analytical predictions of the transverse wall impedance at low frequencies," *Phys. Rev. Spec. Top. Accel. Beams*, vol. 12, no. 8, p. 084 401, 2009. doi:10.1103/PhysRevSTAB.12.084401

[23] C. W. Planner, "Some considerations in the design of an rf shield for ISIS," 1979, SNS/ϕ/n8/79.

[24] L. S. Walling, D. E. McMurry, D. V. Neuffer, *et al.*, "Transmission-line impedance measurements for an advanced hadron facility," *Nucl. Instrum. Methods Phys. Res., Sect. A*, vol. 281, no. 3, pp. 433–447, 1989. doi:10.1016/0168-9002(89)91474-5

[25] A. Macridin, "Coupling impedance and wake functions for laminated structures with an application to the Fermilab Booster," *Phys. Rev. Spec. Top. Accel. Beams*, vol. 14, no. 6, p. 061 003, 2011. doi:10.1103/PhysRevSTAB.14.061003

[26] A. Burov and V. Lebedev, "Impedances of laminated vacuum chambers," Fermi National Accelerator Lab., Batavia, IL, USA, Rep. FERMILAB-TM-2492-AD, Jun. 2011. doi:10.2172/1021483

[27] C. V. Dodd and W. E. Deeds, "Analytical solutions to Eddy-current probe coil problems," Oak Ridge National Lab., TN, USA, Rep. ORNL-TM-1987, Jan. 1967. doi:10.2172/4499902

[28] K. Y. Ng, *Physics of Intensity Dependent Beam Instabilities*. World Scientific, 2005. doi:10.1142/5835

[29] P. Barrat, "The ISIS synchrotron rf system at high intensity," in *12th Meeting of Int. Collaboration on Advanced Neutron Sources (ICANS XII)*. http://www.neutronresearch.com/parch/1993/01/199301031090.pdf

[30] S. Lucyszyn, "Microwave Characterization of Nickel," vol. 4, no. 6, pp. 686–690, 2008. doi:10.2529/PIERS080119215655

[31] H. Hahn, "Impedance measurements of the SNS extraction kicker system," Brookhaben Nationa;l Lab., Upton, NY, USA, Rep. BNL-105704-2014-IR, May 2004. doi:10.2172/1157313

[32] L. Huang, Y. Liu, and S. Wang, "The coupling impedance measurement of the fast extraction kicker in CSNS/RCS," in *Proc. IPAC'15*, Richmond, VA, USA, Jun. 2015. doi:10.18429/JACoW-IPAC2015-MOPWA060

[33] E. Koukovini-Platia, M. Barnes, H. Bartosik, *et al.*, "Source of horizontal instability at the CERN Proton Synchrotron Booster," *Phys. Rev. Spec. Top. Accel. Beams*, vol. 22, no. 12, p. 124 201, 2019. doi:10.1103/PhysRevAccelBeams.22.124201

[34] D. M. Pozar, *Microwave Engineering, 4th Edition*. Wiley Global Education, 2011.

[35] Y. Shobuda, Y. Irie, T. Toyama, *et al.*, "Measurement scheme of kicker impedances via beam-induced voltages of coaxial cables," *Nucl. Instrum. Methods Phys. Res., Sect. A*, vol. 713, pp. 52–70, 2013. doi:10.1016/j.nima.2013.02.037

[36] M. Blaskiewicz and W. Weng, "Transverse instability with large space charge tune shift," Brookhaven National Lab., Upton, NY, USA, Rep. BNL-104796-2014-IR, Sep. 1993. doi:10.2172/1151287

[37] A. W. Chao, *Physics of Collective Beam Instabilities in High Energy Accelerators*, 1st ed. John Wiley & Sons, 1993. http://www.slac.stanford.edu/~achao/wileybook.html

[38] Y. H. Chin, "Transverse mode coupling instabilities in the SPS," CERN, Geneva, Switzerland, Rep. CERN-sps-85-2-di-mst, Feb. 1985. https://cds.cern.ch/record/157995/

[39] A. Burov, "Nested head-tail Vlasov solver," *Phys. Rev. Spec. Top. Accel. Beams*, vol. 17, no. 2, p. 021 007, 2014. doi:10.1103/PhysRevSTAB.17.021007

[40] D. W. Posthuma de Boer, *PyTMCI*, UKRI Science and Technology Facilities Council. https://github.com/stfc/PyTMCI

[41] *PyHEADTAIL*. https://github.com/PyCOMPLETE/PyHEADTAIL